Supporting Information

Charge governed phase manipulation of tellurium few-layers

Cong Wang[1†], Xieyu Zhou[1†], Jingsi Qiao[1], Linwei Zhou[1], Xianghua Kong[1], Yuhao

Pan[1], Zhihai Cheng[1], Yang Chai[2] and Wei Ji[1, *]

[1]*Beijing Key Laboratory of Optoelectronic Functional Materials & Micro-Nano Devices,*

*Department of Physics, Renmin University of China, Beijing 100872, P. R. China*

[2]*Department of Applied Physics, The Hong Kong Polytechnic University, Hung Hom,*

Kowloon, Hong Kong, P. R. China

[†]*These authors contribute equally to this work*

* wji@ruc.edu.cn
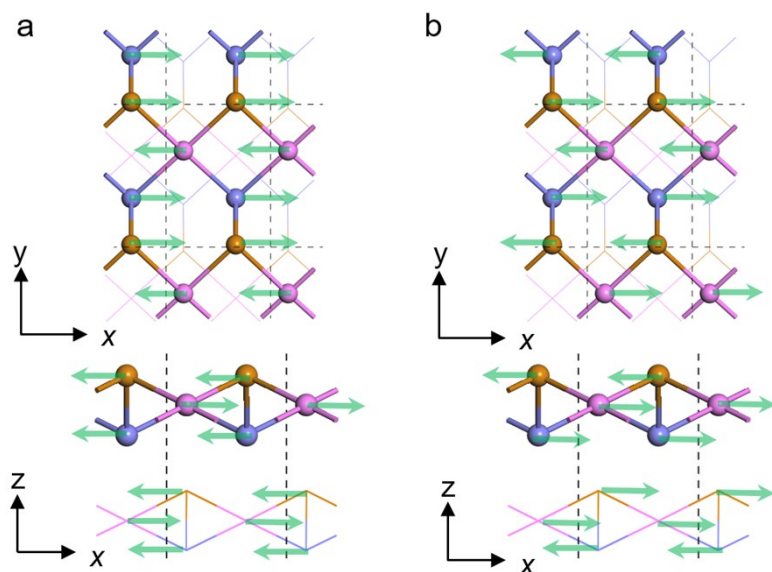
Supplementary Figure S1. Schematic diagrams of vibrational displacements for imaginary vibration modes of bilayer Te in β phase. Figure S1a illustrates the vibrational displacement for the imaginary vibration mode of the neutral bilayer β, which indicates that β-Te is unstable tending to transform to α-Te. Figure S1b shows the vibrational displacement for the imaginary vibration mode appearing with electron doping from 0.04e/Te to 0.1e/Te. Calculations confirmed the stability of l-α+r-α chiral α-Te phase arising from this imaginary vibration mode. The meta-stable l-α+r-α chiral α-Te phase is energetically more stable than other phases except γ phase in a range from 0.04e/Te to 0.1e/Te.
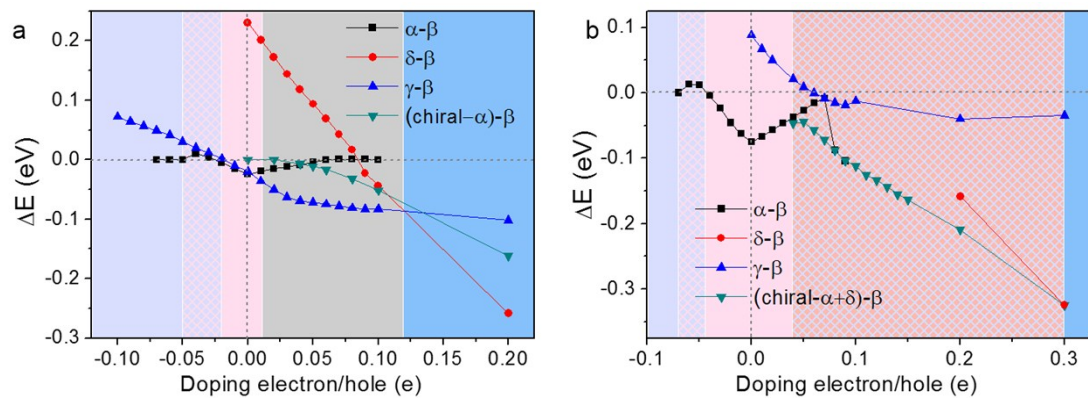
Supplementary Figure S2. Relative total energies of bi- and tri-layer Te in different phases as a function of electron/hole doping level. The total energies of the β-bilayer were chosen as the energy reference and the regions with different colors represent the energetically favored regions for each phase. Four phase transitions in 2L and 3L mentioned in the manuscript can be observed here.
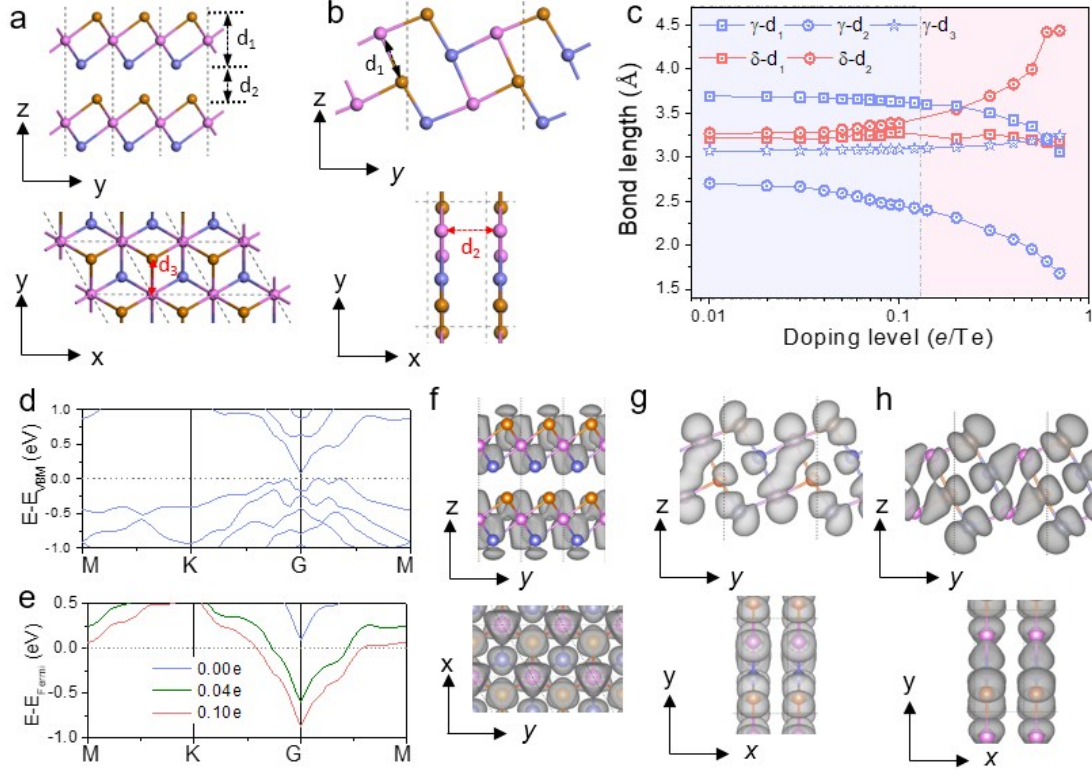
Supplementary Figure S3. Details of the γ-δ phase tansition in a Te bilayer. (a-b) Side-
and Top- views of γ- and δ-Te bilayers. The inter- and intra-layer chain-chain distances and
layer thickness are marked with dashed arrows. (c) The distances marked in a-b as a function
of doping level. The blue region represents the energetically stable region of γ phase and pink
region for the δ phase. (d) Electronic band structure of bilayer Te in γ phase. (e) The
evolution of the bandstructures of the highest valence band (VB) under different charge
doping level. (f) Side- and top-views of the wavefunction norm of the CB state of γ phase at
G using an isosurface of 0.001e Bohr-3. (g-h) Side- and top-views of the wavefunction norm
of the CB state of δ phase at S and X, respectively.

An α-bilayer is unstable and is prone to transform into a β-bilayer upon electron doping.
Both β- and γ-bilayers share the same feature that they are comprised of rhomboid chains, but
in a parallel and a network forms, respectively, as shown in Fig. 1b and 1c. It is thus expectable
that the γ-bilayer (Fig. S4a) shows better stability than the β-bilayer. A metallic δ-bilayer also
looks chain-like but it is comprised of zigzag chains (Fig. S4b). Here, the competition of γ- and
δ-phases is thus highly relevant to the comparison of stability of these chains. We plotted
distances d_1, d_2 and d_3 in Fig. S4c that they reflect the inter-chain couplings among rhomboid
or zigzag chains. In terms of the γ-bilayer, either the layer thickness (d_1, blue squares) or the
interlayer distance (d_2, blue circles) slowly shrinks with respect to the concentration of doped
electrons; this is relevant with the lowest conduction band (CB1) states around the G point
($\psi^\gamma_{CB1,G}$), as indicated in Fig. S4d and S4e. State $\psi^\gamma_{CB1,G}$, an inter-sublayer bonding state (Fig.
S4f), becomes occupied upon electron doping, which strengthens the interactions between the
middle and top/bottom sublayers and thus reduce the layer thickness. The reinforced inter-
sublayer interaction thus keeps the in-plane inter-chain distance (d_3, blue pentagrams) nearly
unchanged up to a level of 0.14 e/Te and slightly increased beyond that level due to a finite
Poisson's ratio. These tendencies of bond-length variations suggest that the rhomboid chains

are still network-like, in different from isolated zigzag chains as δ-bilayer behaves under high doping levels.

The δ-phase coexists with the γ-phase in all considered doping levels. Its CB1 states around the S ($\psi^\delta_{CB1,S}$) and X ($\psi^\delta_{CB1,X}$) points are two anti-bonding states (Fig. S4g and S8h) and are filled under electron doping (see Supplementary Figure S5); this gives rise to continuously elongated intralayer distance d_2 (red circles). In terms of the interlayer region, $\psi^\delta_{CB1,S}$ is a bonding state but $\psi^\delta_{CB1,X}$ is an antibonding one. Distance d_1 is, therefore, nearly unchanged until the doping level reaches 0.8 e/Te. The δ-bilayers can be thus regarded as gradually isolated into six-Te-four-Te chains formed by interlayer bonding. However, γ-bilayers retain a highly distorted rhomboid network where Te-Te bonds are bent, stretched and compressed under doping due to structural constrains in 2D. The constrain in six-four chains in δ-phase is, however, relaxed in the x direction. Therefore, the strain-relaxed six-four chains are energetically more favored under the doping induced strain. These results also suggest that electron doping might be a route of synthesizing δ-Te nanoribbons.
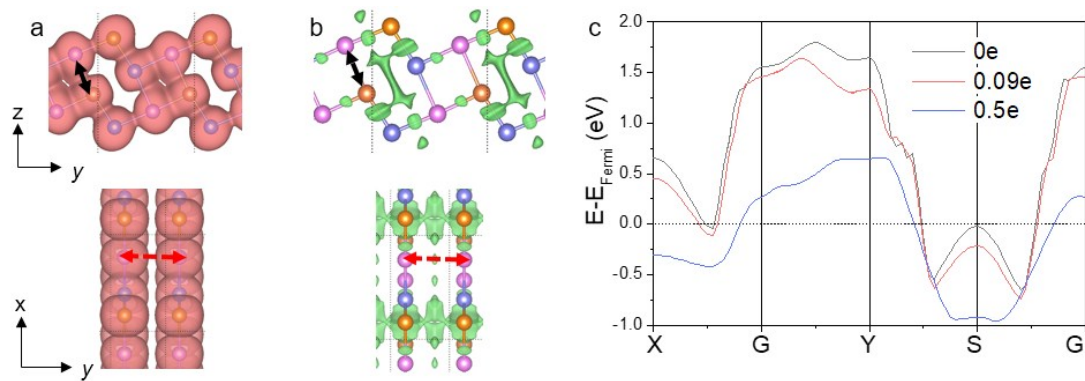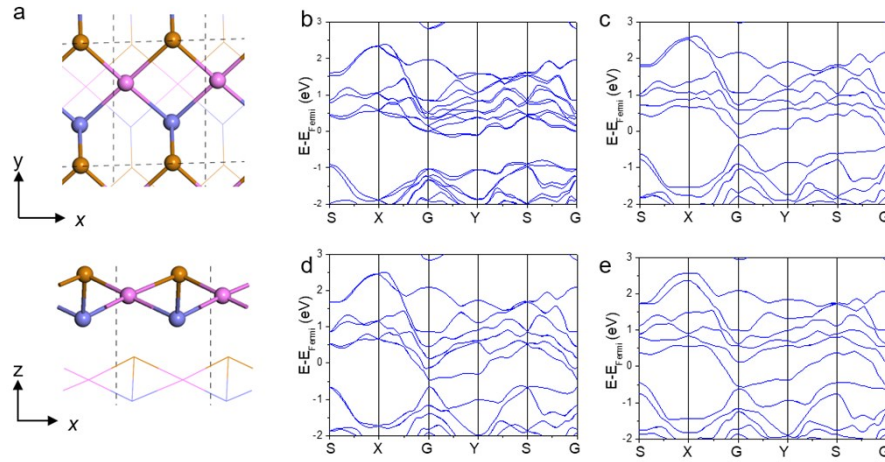

Supplementary Figure S4. Electronic structure of electron doped bilayer Te in δ phase. (a-b) Differential charge density of electron doped bilyer Te-2L-δ using an isosurface of 0.0001e Bohr^{-3}. The red (a) and green (b) isosufacre correspond to the charge accumulation and reduction after electron doping, respectively. Charge accumulation was found along the δ chain and at the interlayer region, which suggested the enhanced interlayer bonding. Charge reduction mainly occurs as the inter-chain region, suggesting the formation of isolated six-Te-four-Te chains. (c) The evolution of the bandstructures near the fermi level under different electron doping level. The CB states around the S ($\psi^\delta_{CB,S}$) and X ($\psi^\delta_{CB,X}$) points are filled by electron doping.
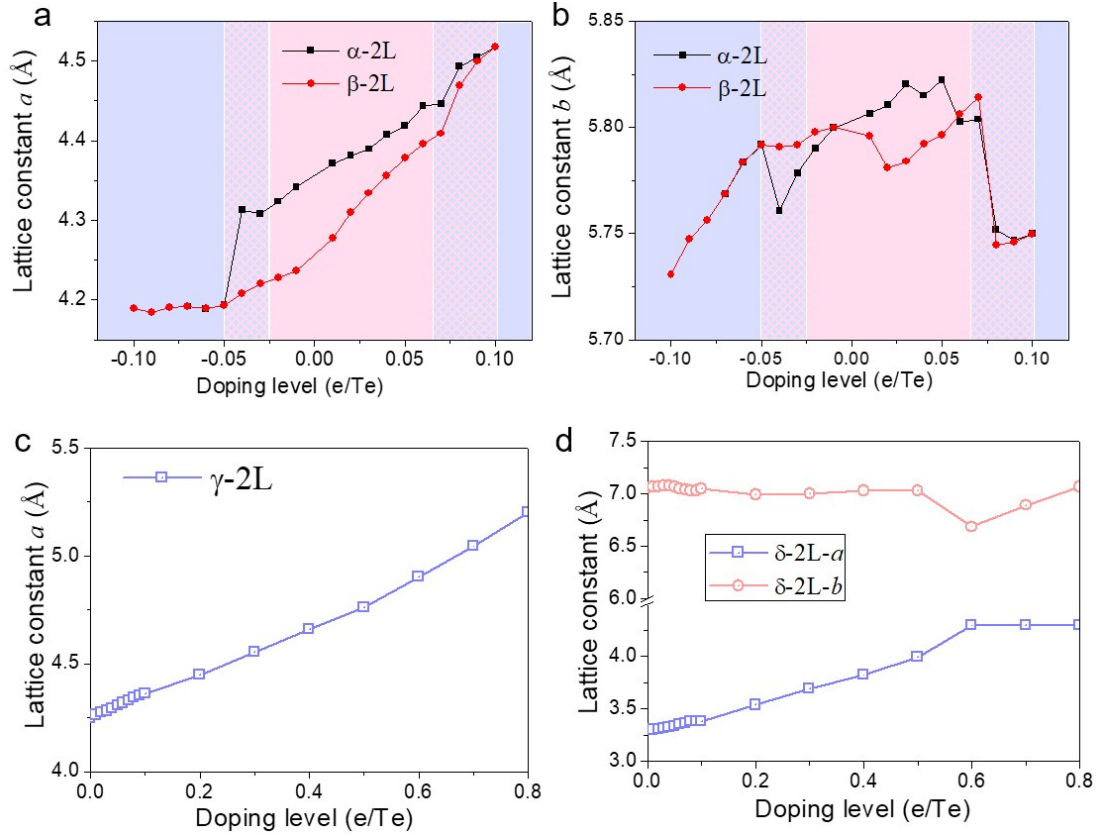
Supplementary Figure S5. Lattice constants of bilayer Te in α, β, γ and δ phase as a function of electron/hole doping level. Figure S6a-b show the lattice constants evolution during the α-β transition. As the increase of the doping level, lattice constant *a* continues expanding, which reflects the strain induce by charge doping. As a result of the varied bond lengths discussed in the manuscript, lattice constant b expands under an electron doping but shrinks in the positively charged region. A slight increase followed with an abrupt drop was found at a hole doping level of 0.04-0.05 h/Te, consistent with the tendency of the bond length changes of Te2-Te3. The *γ*- and *δ*-bilayer show different behavior under electron doping, shown in Figure S6c-d. The *γ* bilayer keeps expending in *xy*-plane as doping level increase, which may attributed to the stain induced by electron doping. As for *δ*-bilayer, the zigzag chain along b-axis maintains but the inter-chain distance (lattice constant *b*) is elongated until doping level exceeding 0.6 e/Te, leading to the isolated zigzag chain.

Supplementary Figure S6. l-α+r-α chiral α-Te in bilayers Te. (a)Top- and side-view of l-α+r-α chiral α-Te bilayer. Atoms in the top layer were represented by balls while thoese in the bottom layer were shown by lines. (b-e) Electronic band structures of electron doped bilayer Te in different phases: (b) α phase under 0.04e/Te, (c) chiral α phase under 0.04e/Te, (d) β pahse under 0.1e/Te, (e) chiral α phase under 0.1e/Te. Electron doped chiral α phase shows similar band structures to β pahse.
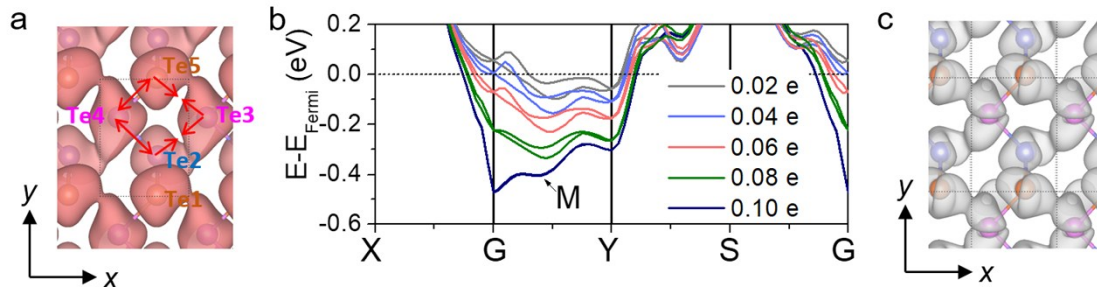
Supplementary Figure S7. Electron doping induced α-β phase tansition in bilayer Te. (a) Differential charge density of electron doped bilyer Te-2L-α using an isosurface of 0.0001e Bohr^{-3}. (b) The evolution of the bandstructures of the lowest conduction band (CB) under different electron doping level. (c) Top view of the wavefunction norm of the CB state of α phase at M. Figure S3a plots an electron doping DCD by a comparison between the densities of a 0.05 e/Te doped and a neutral alpha-Te layers. It indicates an enhanced inter-chain attraction between Te3 and Te2/Te5, although most exceeding charges are located around Te atoms. The DCD could be well explained from the electronic structural point of view. Figure S3b shows the bandstructures of the lowest conduction band (CB) at electron doping levels of 0.02 e/Te to 0.10 e/Te with a step of 0.02e/Te. It turns out that most CB states between the G and Y points are occupied with electron doping. We plotted the wavefunction norm of the lowest CB at the M point ($\psi^a_{CB,M}$) where the CB has the lowest eigenenergy. Figure S7c explicitly shows that $\psi^a_{CB,M}$ is a bonding state of bonds Te2-Te3 and Te3-Te5 and it is occupied from the 0.02 e/Te doping level. Their bond lengths, therefore, exhibit a gradually shortened tendency rather than an abrupt change with respect to electron doping, consistent with the data presented in Fig. 2b.
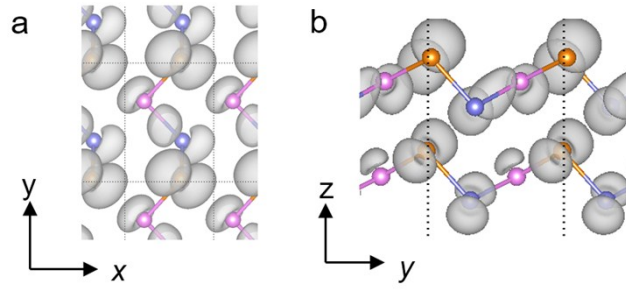
Supplementary Figure S8. Top and side view of the wavefunction norm of the VB state of α phase at the VBM point. At a hole doping level up to 0.04 h/Te, eigenstates of VB were unoccupied between the S and G points of the BZ. These states are neither bonding nor anti-boding states. Thus the bond lengths Te2-Te3 and Te2-Te4 change little as hole doping as shown in Figure 2b.
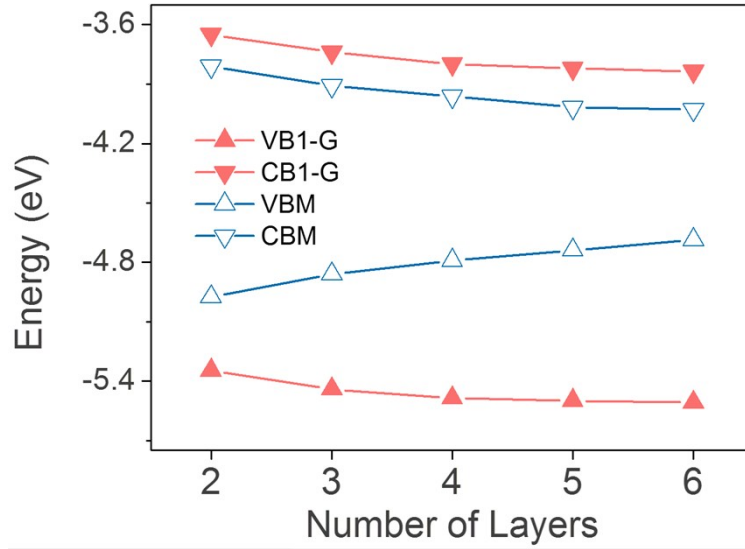
Supplementary Figure S9. Layer-dependent energy levels of CB1 and VB1 states in few-layer α-Te at G point. The energy levels of CBM and VBM reported in ref. science bulletin are also shown here. The values are calculated by HSE06 functional inclusion of SOC and aligned with the vacuum energies. The energy of $\psi^{\alpha}_{VB,G}$ drops from 2L to 3L and 4L, consistent with the enlarged critical doping levels of the α-β transition as shown in Fig. 1e.
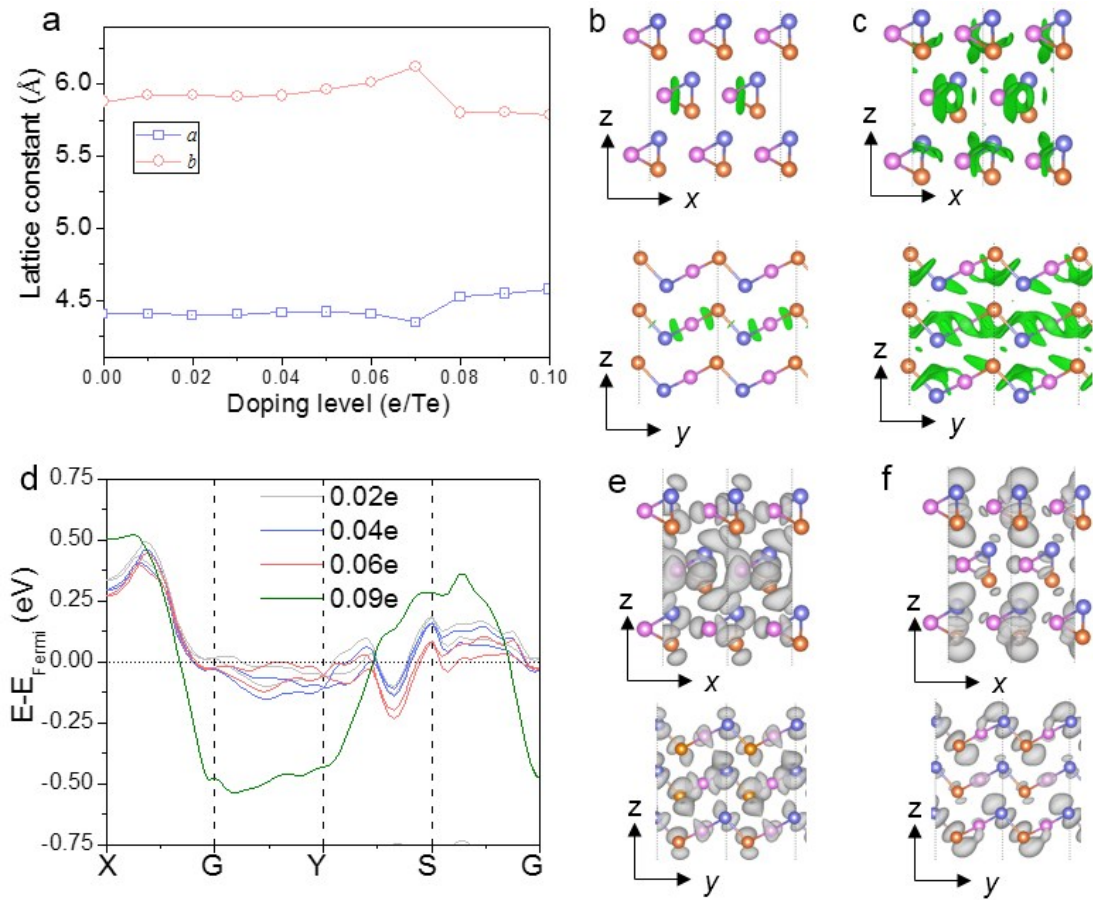
Supplementary Figure S10. Electronic structure of electron doped trilayer Te. (a) The evolution of lattice constants in tri-layer as a function of doping level. The sudden change occurs under a doping level of 0.07e/Te, which is indeed the transition point between α- and mixed phases. (b-c) Side and top views of the differential charge density (DCD) of trilayer Te in α phase with electron dopant concentration 0.02e/Te and 0.04e/Te, respectively. The isosurface is set as 0.00004e Bohr^{-3}. The green isosurface corresponds to the charge reduction after electron doping. (d) The evolution of the bandstructures of the lowest conduction band (CB) under different electron doping level. The CB states around the G and Y points are filled when the doping electron exceeds 0.09 e/Te. (e-f) Side and top view of the wavefunction norm of the CB state of α phase at the G and S point, respectively. Surfaces in trilayer introduces the emergence of central inversion symmetry and chirality, as discussed in the manuscript. The chirality can be observed in both DCD and the wavefunction norm.

Table S1

Relative total energy ΔE per Te atom (with respect to the most stable α phase), lattice constants a and b, interlayer distance d, energy band gaps calculated in neutral bilayer Te. The shape and volume of all phases were fully optimized with optB88-vdW. Electronic band structures were calculated using PBE functional and hybrid functional (HSE06) including spin-orbit coupling (SOC). Neutral α-bilayer is the most stable one with a biggest band gap of 1.17eV. Charge doping can manipulate the transitions between phases with distinct structure forms and band gaps, shedding light on the potential applications for building heterostructures.

phase	Δ E/Te (meV)	a(Å)	b(Å)	d(Å)	E_{Gap}(eV)	
					PBE+SOC	HSE06+SOC
α	0	4.36	5.81	1.88	0.79	1.17
β	4	4.25	5.80	1.97	0.33	0.62
γ	1	4.25	4.25	2.73	0.08	0.26
δ	42	3.30	7.06	1.59	m	m

Table S2

Phase boundaries and corresponding carrier densities in few-layer Te. Surface areas were derived from the optimized structures under certain doping levels. For a phase transition occurred spontaneously, the two phases at the transition point share similar areas and thus show close doping densities. Doping level around 3.0×10^{14} e/cm^2 is usually reachable by ionic liquid gating or intercalation.

2L	Doping Level		3L	Doping Level		4L	Doping Level	
phase	(e/Te)	(10^{14} e/cm^2)	phase	(e/Te)	(10^{14} e/cm^2)	phase	(e/Te)	(10^{14} e/cm^2)
β	-0.03	-0.74	β	-0.04	-1.46	β	-0.07	-3.39
α	-0.03	-0.72	α	-0.04	-1.41	α	-0.07	-3.34
α	0.01	0.24	α	0.08	2.74	α	0.04	1.83
γ	0.01	0.38	chiral-α+δ	0.08	2.74	chiral-α	0.04	1.83
γ	0.13	4.67	chiral-α+δ	0.3	9.66	chiral-α	0.21	9.64
δ	0.13	3.27	δ	0.3	9.66	δ	0.21	9.4

Table S3

As each layer may take left-hand α (l-α), right-hand α (l-α) and δ chains, few-layer Te may have considerable arrangement and combinations. The number of possible phases consist of these three kinds of layers are listed as follow. As the number of layer increases, the diversity of phases increases rapidly and reaches 25 for 4L.

Number of layers	Number of phases
1	2
2	4
3	10
4	25
5	70
6	196
7	574
8	1681

Table S4

Evolution of frequency (cm^{-1}) as a function of doping level for bilayer in α, β, γ phases. The frequencies of Raman activated modes in bilayer α and γ exhibit red-shift under electron doping and nearly unchanged with hole doping. Bilayer β shows similar trend except an anomalous blue-shift for the mode A_1^6. In terms of electron doped bilayer γ, the frequency of the mode A_1^4 is still much higher than modes A_1^{12} and A_1^{11} in α. The distinct indictors maintains under charge doping and keeps useful for experimental identification of these phases.

phase	β				α				γ		
Doping level (e/Te)	A_1^6	A_1^8	A_1^{10}	A_1^{11}	A_1^5	A_1^7	A_1^{11}	A_1^{12}	E^3/E^4	A_1^1	A_1^4
-0.06	95.3	111.0	136.5	148.4	1-	-	-	-			
-0.04	94.5	108.8	136.3	146.5	89.5	114.2	147.1	148.0	83.9	105.5	179.2
0.00	96.3	106.9	137.3	148.3	89.8	118.4	145.4	147.5	85.5	104.7	177.4
0.04	92.1	100.8	126.2	140.5	84.4	112.9	131.7	139.3	45.2	99.5	170.3
0.06	96.9	99.6	123.6	139.6	81.0	106.0	132.7	134.7			

[1] transform into the β phase.

Table S5

Evolution of frequency (cm^{-1}) for the 0.06h/Te doped β bilayer, neutral α bilayer and 0.04e/Te doped γ bilayer as a function of uniaxial strains along the x (*a*) and y (*b*) directions. In-plane strain applied to 2D layers is usually less than 2%. We thus considered the shifts frequency of those Ramon modes under uniaxial strains. It shows that the in-plane strain has little effect on the position of characteristic peaks of α, β and γ phases (with shifts of few cm^{-1}).

phase	0.06h/Te doped β				neutral α				0.04e/Te doped γ		
Strain along x	A_1^6	A_1^8	A_1^{10}	A_1^{11}	A_1^5	A_1^7	A_1^{11}	A_1^{12}	E^3/E^4	A_1^1	A_1^4
-2%	94.7	111.1	137.0	148.3	-[2]	-	-	-	71.6	103.5	173.5
-1%	94.6	109.6	135.8	148.0	89.4	117.3	146.5	147.9	69.8	102.2	171.8
0%	95.3	111.0	136.5	148.4	89.8	118.4	145.4	147.5	45.2	99.5	170.3
1%	-[1]	-	-	-	90.4	120.2	144.8	147.7	63.8	99.5	171.2
2%	-	-	-	-	90.5	121.3	145.2	147.7	78.8	100.5	170.9

phase	0.06h/Te doped β				neutral α			
strain along y	A_1^6	A_1^8	A_1^{10}	A_1^{11}	A_1^5	A_1^7	A_1^{11}	A_1^{12}
-2%	96.1	110.1	139.0	148.5	91.9	119.4	148.8	150.0
-1%	95.3	109.6	137.7	148.0	90.8	119.1	147.3	149.3
0%	95.3	111.0	136.5	148.4	89.8	118.4	145.4	147.5
1%	93.6	109.9	135.3	147.5	89.6	118.4	143.6	145.4
2%	92.7	109.4	133.9	146.9	89.1	118.4	144.9	145.4

[1] transform into the α phase. [2] transform into the β phase.

Table S6

Lattice constants of the α-, β-, γ- and δ-phases as a function of number of layers. Given these lattice constants, we have several statements as follows. (1) Tensile strain along the *a* axis could stabilize the α-phase in 1L and defer the boundary for the α-β transition in 2L or thicker layers. (2) Compressive strain along that direction may lead to the appearance of the neutral β-phase in 2L or thicker layers and advances the transition boundaries. (3) Biaxial compressive strain should promote the stability of the γ-phase since it has the smaller surface area per Te. (4) Large tensile strain along the *b* axis results in the δ-phase being the most energetically favored one among these four phases. These results suggest that bi- or uniaxial effective pressure could be another route to tune the stability of these phases.

Phase	α			β			γ		δ		
N_{Layer}	a (Å)	b (Å)	S(Å²)	a (Å)	b (Å)	S(Å²)	a (Å)	S(Å²)	a (Å)	b (Å)	S(Å²)
1	-	-		4.22	5.58	23.55	4.22	15.42	3.03	6.35	19.24
2	4.36	5.81	25.33	4.25	5.80	24.65	4.25	15.64	3.30	7.05	23.26
3	4.40	5.88	25.87	4.26	5.88	25.05	4.27	15.79	3.26	7.16	23.34
4	4.42	5.91	26.12	4.27	5.92	25.28	4.28	15.86	3.22	7.00	22.54
5	4.44	5.93	26.33	4.28	5.94	25.42	4.34	16.31	3.23	7.02	22.67
6	4.44	5.94	26.37	4.28	5.95	25.47	4.57	18.09	3.23	7.04	22.74